



Enhancing photocatalytic activity of tantalum nitride by rational suppression of bulk, interface and surface charge recombination

Mu Xiao, Zhiliang Wang, Bin Luo, Songcan Wang, Lianzhou Wang*

Nanomaterials Centre, School of Chemical Engineering and Australian Institute for Bioengineering and Nanotechnology (AIBN), the University of Queensland, St Lucia, QLD, 4072, Australia

ARTICLE INFO

Keywords:

Tantalum nitride
Hollow structure
Doping
Co-catalyst
Surface passivation

ABSTRACT

Rational design of photocatalysts is essential to achieve efficient solar energy conversion. For narrow bandgap Ta_3N_5 photocatalyst, various charge recombination occurring in the bulk, interface and on the surface significantly impairs its activity for solar hydrogen (H_2) generation. Herein, a synergistic engineering approach is designed to solve this critical recombination challenge. First, hollow spherical structure of Ta_3N_5 with Mg doping is prepared to not only reduce the charge migration distance and increase the surface area, but also increase the electron mobility for facilitated charge transfer. Second, an MgO nano-layer covers the surface of hollow Ta_3N_5 structure to passivate surface defects, thus promoting the interfacial charge transfer between Ta_3N_5 and co-catalysts. Finally, dual co-catalysts (Pt/CoO_x) for redox reactions are loaded onto the hollow Ta_3N_5 structure to reduce the surface recombination and overcome the sluggish surface reaction. Remarkably, the combination of hollow structure, Mg^{2+} doping, MgO interfacial layer, and dual co-catalysts effectively improves the charge separation and transfer in Ta_3N_5 photocatalyst. This newly designed photocatalyst exhibits a considerably improved H_2 generation performance of $56.3 \mu\text{mol h}^{-1}$ under simulated sunlight, compared to that of reference $\text{Pt}/\text{Ta}_3\text{N}_5$ hollow spheres.

1. Introduction

Photocatalytic water splitting is considered as a highly attractive approach to convert abundant solar energy into clean fuels [1–4]. Tantalum nitride (Ta_3N_5) is a promising photocatalyst for H_2 generation due to its ideal narrow bandgap ($\sim 2.1 \text{ eV}$) and sufficient redox potentials for both H_2 and O_2 evolution [5–7]. The conduction band minimum (CBM) of Ta_3N_5 is $\sim 0.3 \text{ eV}$ negative than the water reduction potential while the valence band maximum (VBM) is around 0.5 eV positive than the water oxidation potential [8]. The theoretical STH efficiency of Ta_3N_5 is $\sim 15.9\%$ according to the bandgap theory [9]. However, the experimental performance of Ta_3N_5 photocatalyst is severely limited by the charge recombination in bulk, interface and on surface due to its intrinsic drawbacks, including low carrier mobility, bulk and surface defects, and slow surface kinetics [10]. The carrier mobility is in the range of $1.3\text{--}4.4 \text{ cm}^2 \text{ V}^{-1} \text{ s}^{-1}$ and lifetime of photo-generated charge carriers is as short as 10 ps in pristine Ta_3N_5 [11]. On the other hand, nitrogen vacancies (N_V) and reduced Ta species resulted from NH_3 treatment in the common photocatalyst preparation process creates interfacial barrier between Ta_3N_5 and co-catalysts, leading to worsened charge transfer efficiency [12]. In addition, such defects also

promote the surface charge recombination [13]. Furthermore, the lack of active sites on the surface of Ta_3N_5 results in sluggish redox reactions, inducing the accumulation of charge carriers for recombination [12]. All these factors are highly deteriorating to the photocatalytic process on this promising photocatalyst. How to effectively address the charge recombination problems in Ta_3N_5 photocatalyst to fully release its solar H_2 production potential remains challenging.

A number of strategies have been developed to improve the charge separation and transportation in Ta_3N_5 for efficient solar H_2 generation, while most of the studies were concerned about one or two recombination problems [7]. Generally, construction of nanostructures and doping are two effective approaches to reduce bulk recombination [14,15]. Up to date, Ta_3N_5 photocatalysts with various nanostructures, including hollow spheres, nanosheets, nanorods/nanotubes, and nanoparticles have been developed to shorten the charge transfer distance, thus reducing bulk recombination [16–20]. Meanwhile, metal dopants such as Na, Mg, K, Rb, Cs, Zr and W have been explored to tune the electronic structure of Ta_3N_5 for improved conductivity and transportation of charge carriers [18,21,22]. Some recent studies reveal that the coating of some metal oxide layers on the surface of Ta_3N_5 could effectively passivate surface defects and improve the charge transfer

* Corresponding author.

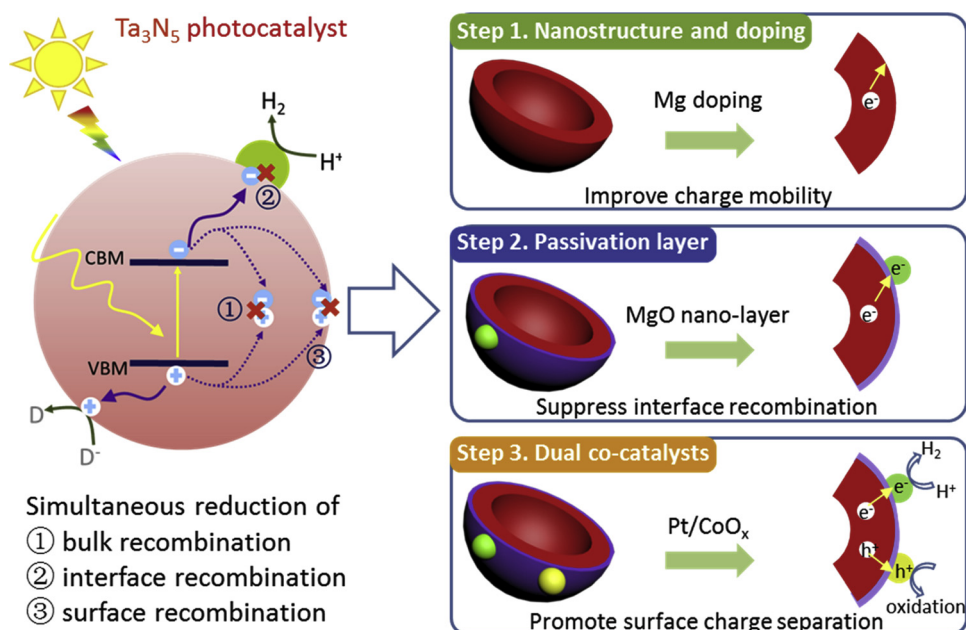
E-mail address: l.wang@uq.edu.au (L. Wang).

<https://doi.org/10.1016/j.apcatb.2019.01.053>

Received 8 October 2018; Received in revised form 10 January 2019; Accepted 18 January 2019

Available online 19 January 2019

0926-3373/© 2019 Published by Elsevier B.V.



Scheme 1. Schematic illustration of various charge recombination problems in Ta₃N₅ photocatalyst and the corresponding synergistic approach to solve those problems. Red: Ta₃N₅, purple: MgO nano-layer, green: Pt, yellow: CoO_x. (For interpretation of the references to colour in this Scheme legend, the reader is referred to the web version of this article.)

between co-catalysts and Ta₃N₅ [23,24]. To promote surface charge separation and accelerate surface reactions, loading dual co-catalysts for redox reactions (Pt/CoO_x, Pt/IrO₂) have also been attempted [12,25]. Despite intensive efforts over the past years, research on Ta₃N₅ photocatalyst for solar H₂ generation progresses at a slow pace, and the reported photocatalytic H₂ evolution activities are still moderate. This can be easily understood, as no strategies yet can effectively address all the charge recombination problems of Ta₃N₅ photocatalyst. Thus, the combination of various strategies is highly desirable to achieve outstanding photocatalytic performance.

Herein, a synergistic three-step engineering approach is reported to design an efficient Ta₃N₅ photocatalyst by simultaneously suppressing the charge recombination in bulk, interface and on surface. The function of this three-step approach is schematically illustrated in Scheme 1. The first step is to reduce the bulk recombination of Ta₃N₅. Hollow-spherical morphology with thin shell is fabricated to decrease the charge migration distance. Meanwhile, Mg²⁺ ions are doped into Ta₃N₅ to increase the charge mobility. The second step is to suppress the interfacial recombination. An interfacial nano-layer of MgO covers the surface of hollow Mg-Ta₃N₅ structure to improve the charge transportation between Ta₃N₅ and co-catalysts. The final step is to reduce the surface recombination. Dual co-catalysts for reduction (Pt) and oxidation reactions (CoO_x) are decorated on the surface to promote surface charge separation and accelerate surface redox reactions. Consequently, due to the efficient separation and transfer of photo-generated electron-hole pairs, the new Ta₃N₅ based photocatalyst exhibits remarkably enhanced photocatalytic H₂ production compared with its bulk counterpart.

2. Experimental section

2.1. Preparation of carbon spheres as template

Carbon spheres were prepared using a modified hydrothermal method [26,27]. In a typical process, 60 mL of 10 wt.% glucose (99.5%, Sigma-Aldrich) aqueous solution was sealed in a 100 mL Teflon-lined autoclave and then kept at 433 K for 6 h in an oven. After cooling down naturally, brown products were collected by centrifuging at 10,000 rpm for 5 min, which were further washed with water and ethanol for several times, respectively. The precipitate was dried in a vacuum oven at 333 K for 12 h before use.

2.2. Mg-doped Ta₂O₅ hollow spheres synthesis

Mg-doped Ta₂O₅ hollow spheres were prepared with carbon spheres as hard template [27,28]. TaCl₅ (99.8%, Sigma-Aldrich) and Mg(NO₃)₂·6H₂O (99%, Sigma-Aldrich) with a ratio of 20 were dissolved in 100 mL of absolute ethanol. Next, 500 mg of carbon spheres were added into the solution with ultrasonication for 1 h, then kept stirring for 6 h at room temperature. After that, the mixture was centrifuged and washed with ethanol for 3 times to remove the residue of metal salts. After drying, carbon spheres were removed through calcination in air at 773 K for 8 h. The obtained Mg doped Ta₂O₅ hollow spheres were named as Mg-Ta₂O₅. The concentration of Mg dopants can be easily tuned by varying the ratio of TaCl₅ and Mg(NO₃)₂·6H₂O in the solution. For comparison, Ta₂O₅ hollow spheres were prepared following the same procedure without Mg(NO₃)₂·6H₂O in the solution.

2.3. Surface modification of hollow spheres with MgO nano-layer

MgO nano-layer was covered on the surface of hollow spheres through an in-situ method [24]. Typically, Mg-Ta₂O₅ hollow spheres was immersed in a MgSO₄ (99.5%, Sigma-Aldrich) aqueous solution. Next, the water was evaporated in a oil bath at 353 K. After calcining the dried mixture at 973 K for 1 h in air, the formed MgO/Mg-Ta₂O₅ hollow spheres were treated under an NH₃ flow (100 mL min⁻¹) at 973 K for 6 h, producing a MgO/Mg-Ta₃N₅ sample [19]. For comparison, MgO/Ta₃N₅ hollow spheres were also prepared by using Ta₂O₅ hollow spheres. The bulk Ta₃N₅ was prepared by nitriding the commercial Ta₂O₅ powder under NH₃ flow at 1173 K for 15 h [5].

2.4. Deposition of dual CoO_x (2 wt%) and platinum (1 wt%) co-catalysts

Cobalt oxide (CoO_x) was loaded on the surface of MgO/Mg-Ta₃N₅ hollow spheres as an oxygen evolution co-catalyst by an impregnation method [12]. First, calculated amount of cobalt nitrate (99.5%, Sigma-Aldrich) aqueous solution was impregnated on the surface of hollow spheres by evaporating the water. Then as-prepared sample was put into a tube furnace and annealed at 973 K for 1 h with 100 mL min⁻¹ of ammonia gas flow to obtain the CoO_x loaded photocatalysts. For platinum loading, an in-situ photodeposition method was applied [29]. A calculated amount of H₂PtCl₆ was added into methanol aqueous solution (10 vol%) which contained certain amount of CoO_x/MgO/Mg-

Ta₃N₅ powder. The mixture was illuminated under simulated sunlight for 1 h. After H₂ signal was detected by the gas chromatography (GC), the system was vacuated thoroughly and H₂ evolution reaction started.

2.5. Characterization

X-ray diffraction (XRD) and Raman were performed to identify the crystal structures of various samples. Scanning electron microscope (SEM), transmission electron microscope (TEM) and high-resolution TEM (HRTEM) were operated to explore the microstructures and morphologies of various samples. The concentration of Mg dopants in Ta₃N₅ and the weight ratio of MgO nano-layer on Ta₃N₅ hollow spheres were quantified by energy-dispersive X-ray spectroscopy (EDS) and inductively coupled plasma optical emission spectrometry (ICP-OES). N₂ adsorption and desorption was adopted to measure the specific surface areas of samples based on the Brunauer-Emmett-Teller (BET) theory. X-ray photoelectron spectroscopy (XPS) measurement was conducted to investigate the chemical component and chemical states of various samples. The results were calibrated by the C 1 s peak with a binding energy of 284.8 eV. Photoluminescence spectroscopy and ultraviolet-visible (UV–vis) light absorption spectra were used to explore the optical properties of samples. As for the lifetime measurement, the samples were excited by a 377 nm laser at room temperature.

2.6. Photoelectrochemical measurement

The electrode was prepared by using an electrophoretic deposition method [30,31]. Typically, 20 mg of sample powder and 10 mg of iodine were dispersed in 20 mL of acetone through ultrasonication for 20 min. Then, the electrophoretic deposition process was performed between a piece of FTO glass and Ti foil with a distance of 1 cm. A 20 V bias was applied for 2 min during the process. The powder sample was coated on Ti foil with an area of around 1 cm × 1 cm. After dried in air, 10 μL of TaCl₅ ethanol solution was dropped on the electrode and then dried naturally. After repeating this neking process for five times, the electrode was calcined at 823 K for 1 h under NH₃ flow and cooled down naturally.

All the electrochemical tests were operated in a three-electrode system with 1 M NaOH aqueous solution as electrolyte. The Mott-Schottky curve was collected in dark at 1000 Hz with a scan rate of 20 mV. The linear sweep voltammetry curve was collected in a CHI 660d electrochemical work station with a scan rate of 50 mV.

2.7. Photocatalytic hydrogen evolution reaction

Photocatalytic reaction was performed on the Labsolar-III AG system (Beijing Perfectlight Technology co. LTD). In detail, the reaction system is composed of a Pyrex reaction cell and a gas evacuation&circulation system, which is connected with a GC. For hydrogen evolution reaction, 50 mg of the sample was dispersed in 100 mL of methanol aqueous solution (10 vol. %). After vacuumizing the reaction cell for several times, the reaction cell was irradiated under simulated sunlight. To eliminate the thermal effect caused by lamp, the temperature of reaction cell was kept at 277 K by a water cooling jacket during reaction. The evolved gas was carried into GC for analysis.

The apparent quantum efficiency (AQE) was evaluated by following the equation (Eq.) below: [16]

$$\text{AQE} = \frac{2 \cdot R}{I} \times 100\% \quad (1)$$

R and I are the amount of generated H₂ molecules and the incident photons during the same period, respectively. The light source was a 300 W xenon lamp with a 400 nm band-pass filter. The intensity of light was measured by putting a thermopile on the bottom of reactor. The other conditions for reaction were kept the same as the photocatalytic H₂ evolution test.

3. Results and discussion

The preparing procedure of Ta₃N₅ photocatalyst is schematically shown in Fig. S1 (ESI†). To begin with, Mg-doped Ta₂O₅ (Mg-Ta₂O₅) hollow spheres were synthesized by using a hard-template method with carbon spheres (Fig. S2, ESI†) as the template [28]. With a calculated amount of Mg(NO₃)₂ and TaCl₅, the concentration of Mg dopant was optimized based on the photocatalytic performance of the samples [22,32]. As demonstrated in the Fig. S3, (ESI†), the Pt/Mg-Ta₃N₅ photocatalyst with ~2 at.% Mg-dopant demonstrated the best photocatalytic evolution performance, which was subsequently used as an optimal doping concentration for the following studies. Next, a MgO nano-layer covered the surface of Mg-Ta₂O₅ hollow spheres and MgO/Mg-Ta₂O₅ hollow spheres were converted into MgO/Mg-Ta₃N₅ hollow spheres by the thermal treatment under NH₃ gas flow [24]. The amount of MgO was optimized based on the photocatalytic H₂ production performance and fixed at ~2 wt. % in the sample (Fig. S4, ESI†). It is clear that a certain amount of MgO is important to cover the surface of Ta₃N₅, while too much MgO may impede the charge transfer due to the poor conductivity of MgO [23]. After that, the CoO_x (2 wt. %) and Pt co-catalysts (~1 wt. %) were loaded on the surface of MgO/Mg-Ta₃N₅ hollow spheres successively [12]. The element composite of various samples were identified using inductively coupled plasma optical emission spectrometry (ICP-OES) and summarized in Table S1 (ESI†).

The crystal structures and chemical composite is fundamental for a photocatalyst. The crystal structure of all samples were examined by XRD (Fig. 1). All diffraction peaks of the pure Ta₃N₅ hollow spheres can be assigned to the monoclinic phase of Ta₃N₅ (PDF#65-1247), indicating the full conversion of Ta₂O₅ into Ta₃N₅ [5]. As for Mg-Ta₃N₅ hollow spheres, the XRD pattern is coincident with that of pure Ta₃N₅ and no visible peaks belonging to MgO are detected. Furthermore, Raman spectroscopy was adopted to study the microstructures of Ta₃N₅ photocatalysts (Fig. S5, ESI†). Mg-Ta₃N₅ reveals similar characteristics of the Raman spectra with Ta₃N₅ does, without the characteristic signal of separated MgO phase detected [33]. Based on the above results, it is reasonable to claim that the majority of Mg²⁺ species is doped, or substituted, into the Ta₃N₅ framework rather than forming secondary phase (e.g. MgO). As for the samples with MgO nano-layer (MgO/Ta₃N₅

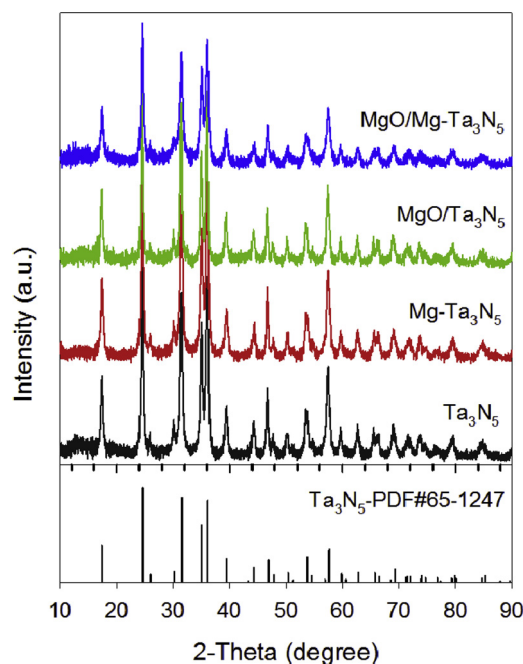


Fig. 1. XRD patterns of samples Ta₃N₅, Mg-Ta₃N₅, MgO/Ta₃N₅ and MgO/Mg-Ta₃N₅ hollow spheres.

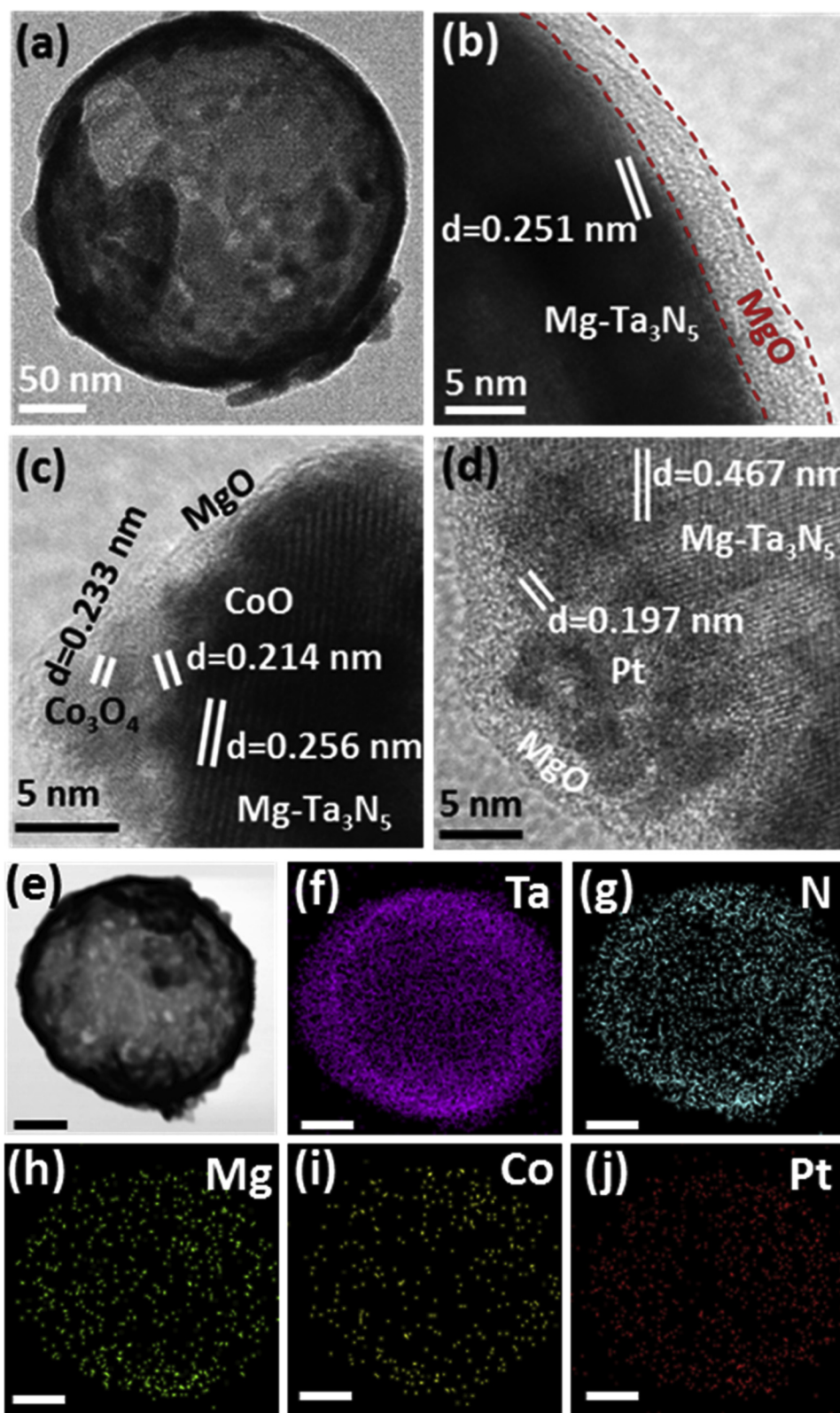


Fig. 2. (a–d) TEM and HRTEM images of (a) $\text{Mg-Ta}_3\text{N}_5$, (b) $\text{MgO/Mg-Ta}_3\text{N}_5$ (c) $\text{CoO}_x/\text{MgO/Mg-Ta}_3\text{N}_5$ and (d) $\text{Pt/CoO}_x/\text{MgO/Mg-Ta}_3\text{N}_5$ hollow sphere. (e–i) EDS elemental mapping images of sample $\text{Pt/CoO}_x/\text{MgO/Mg-Ta}_3\text{N}_5$. The scale bar is 100 nm.

and $\text{MgO/Mg-Ta}_3\text{N}_5$), there are no peaks belong to MgO detected, possibly due to the low content of MgO (Fig. 1).

In addition to crystal structure, morphology is another important factor that will influence the performance of photocatalysts. According to the SEM images, all samples show similar spherical morphology with

diameter ranging from 100 nm to 300 nm (Fig. S6 ESI[†]), demonstrating the well maintenance of spherical morphology after the coating of MgO nano-layer. Meanwhile, there is no significant decrease for the specific surface area after multi-step procedure (Table S2, ESI[†]). TEM image further verifies the hollow spherical feature in the samples with a shell

thickness of about 10 nm (Fig. 2a). From the viewpoint of photocatalytic reaction, this ultrathin shell structure should have the advantages including short diffusion distance for photo-generated carriers in this shell structure to greatly reduce the recombination opportunity and abundant active sites provided by the large surface area ($125 \text{ m}^2 \text{ g}^{-1}$, Fig. S7, ESI†) [19,34,35]. The deposited MgO nano-layer covers the surface of Mg-Ta₃N₅ hollow spheres well with a thickness less than 5 nm (Fig. 2b), which should be thin enough to guarantee an excellent charge transportation between Mg-Ta₃N₅ and co-catalysts. As shown in Fig. 2c, the distance of lattice fringes are assigned to CoO (0.214 nm) and Co₃O₄ (0.256 nm), respectively, which confirms the components of CoO_x [12]. The HRTEM image in Fig. 2d demonstrates the deposition of Pt nanoparticles with an average size of around 2 nm [12]. The EDS mapping (Fig. 2e–j) of a single hollow sphere particle shows the homogeneous distribution of Ta, N, Mg, Co and Pt elements in the sample, indicating the uniform dispersion of Mg²⁺ dopants, MgO passivation layer, CoO_x cocatalyst and Pt cocatalyst on the Ta₃N₅ hollow spheres.

Due to the surface-reaction nature, the surface chemical states of a photocatalyst plays an essential role in photocatalytic activity. Thus, surface chemical states of different Ta₃N₅ photocatalysts were examined using X-ray photoelectron spectroscopy (XPS). The high-resolution XPS spectra of Ta 4f peak and N 1s peak for various samples further confirm the existence of Ta₃N₅ (Fig. S8 ESI†) [16]. Furthermore, the chemical states of Mg and O for Mg-Ta₃N₅, MgO/Ta₃N₅ and MgO/Mg-Ta₃N₅ were investigated (Fig. 3a). All of those samples show obvious Mg 1s peak, confirming the existence of Mg element in the samples [22,30]. Compared with MgO/Ta₃N₅ and MgO/Mg-Ta₃N₅, the Mg 1s peak for Mg-Ta₃N₅ is much weaker, which can be explained by the relatively low doping concentration. The O 1s peak is split into two peaks, corresponding to the binding energy of O²⁻ and OH⁻, respectively (Fig. 3b) [23]. The O²⁻ peak in Mg-Ta₃N₅ is from the substitution of N³⁻ with O²⁻, which is caused by Mg²⁺ dopants [36]. In addition, the O²⁻ peak of Mg-Ta₃N₅ shifts to lower regions compared with MgO/Ta₃N₅. The lower binding energy can be attributed to the lower electronegativity of Mg²⁺ ions compared with that of Ta⁵⁺ ions [24]. Compared with Mg-Ta₃N₅, the OH⁻ peaks of MgO/Ta₃N₅ and MgO/Mg-Ta₃N₅ exhibit much higher intensity, resulting from the conversion of MgO to Mg(OH)₂ when exposing to water [23]. The OH⁻/O²⁻ ratios derived from the XPS of O 1s peaks are 0.26, 2.38 and 1.7 for Mg-Ta₃N₅, MgO/Ta₃N₅ and MgO/Mg-Ta₃N₅, respectively, indicating the influence of different Mg species on O species. For Pt/CoO_x/MgO/Mg-Ta₃N₅, the presence of Pt and Co has also been confirmed (Fig. S9 ESI†). According to the binding energy of Co 2p_{3/2} (782.8 eV) and Co 2p_{1/2} (797.8 eV), the loaded cobalt complex is demonstrated to be the mixture of both Co²⁺ and Co³⁺ (donated as CoO_x for simplicity) [12,24].

According to the above characterization and analysis, it is reasonable to claim that the expected Ta₃N₅ photocatalyst, namely Pt/CoO_x/MgO/Mg-Ta₃N₅ hollow spheres, has been obtained. Then, the optical

and electrical properties of various samples were investigated using UV-vis light absorption spectroscopy, photoluminescence spectroscopy and electrochemical measurement. Pure Ta₃N₅ hollow spheres displays an absorption edge situated at ~590 nm, which corresponds to a band gap of 2.1 eV (Fig. S10, ESI†) [5,8]. Upon Mg-doping, the Mg-Ta₃N₅ and MgO/Mg-Ta₃N₅ exhibit similar light absorption edge as Ta₃N₅. To further understand the optical property, the fluorescence lifetime of all samples are characterized and the lifetime of all samples has been summarized in Table S3 (ESI†). As shown in Fig. 4a, the fluorescent intensities of all samples exhibit an exponential decay. Compared with Ta₃N₅, the lifetime of MgO/Ta₃N₅ is almost unchanged. However, the Mg-Ta₃N₅ and MgO/Mg-Ta₃N₅ samples show remarkably longer lifetime, suggesting that the introduction of Mg²⁺ ions into Ta₃N₅ prolongs the fluorescent lifetime. The prolonged radiative lifetime indicates enhanced possibility for photo-generated charge carriers to participate into redox reactions.

To gain deep insight into the effect of Mg dopants on charge separation and transfer for Ta₃N₅ photocatalyst, the electrochemical measurement was taken out for Mg-Ta₃N₅. As shown in Fig. 4b, the positive slope of Mott-Schottky (MS) curve indicates that Ta₃N₅ remains its n-type nature after Mg doping [22,30]. The flat band potential for both Ta₃N₅ and Mg-Ta₃N₅ are ~0.18 V vs. RHE, extracted from the MS curves. The carrier concentration can be calculated by the following Eq. (2): [30]

$$N_d = \frac{2}{e\epsilon_0\epsilon} \times \left[\frac{d\left(\frac{1}{C^2}\right)}{dV_s} \right]^{-1} \quad (2)$$

Where N_d , e , ϵ , ϵ_0 , C and V_s represent the donor density, the electron charge, the dielectric constant, the permittivity of vacuum, space charge capacitance in the semiconductor and applied potential for MS measurement, respectively. It is assumed that the values of e , ϵ , ϵ_0 keep the same for Ta₃N₅ and Mg-Ta₃N₅. Therefore, the smaller value of C^{-2} for Mg-Ta₃N₅ demonstrates the higher electron density of Mg-Ta₃N₅ than that of Ta₃N₅ under the same bias potential. Theoretically, Mg²⁺ should act as an electron acceptor in Ta₃N₅. However, the replacement of Ta⁵⁺ by Mg²⁺ leads to the substitution of N³⁻ by O²⁻ [36]. It has been regarded that the formed O²⁻ defects not only acted as shallow donor in Ta₃N₅ to provide electrons with high mobility, but also decrease the amount of nitrogen vacancies to reduce the charge recombination centres [30,36]. Therefore, Mg²⁺ dopants enhance the electron concentration and reduce the bulk recombination by introducing O²⁻ defects, both of which improve the bulk charge separation and transfer. In addition, Mg-Ta₃N₅ exhibits higher photocurrent than that of Ta₃N₅, which further confirms the positive effect of Mg dopants on Ta₃N₅ photocatalyst (Fig. S11 ESI†).

In addition, the influence of MgO nano-layer on the charge transfer at the interface was studied. The particle sizes of Pt on Pt/Ta₃N₅ (bulk), Pt/Ta₃N₅ hollow spheres and Pt/MgO/Ta₃N₅ hollow spheres were

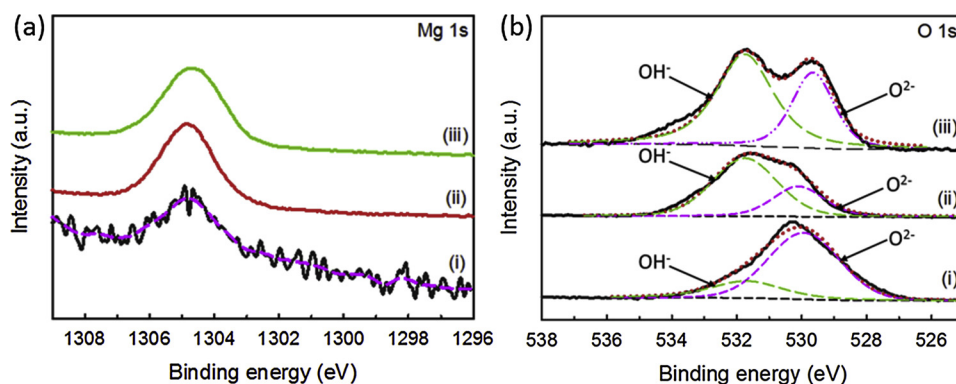


Fig. 3. XPS narrow spectra of samples (i) Mg-Ta₃N₅, (ii) MgO/Ta₃N₅ and (iii) MgO/Mg-Ta₃N₅: (a) Mg 1s and (b) O 1s.

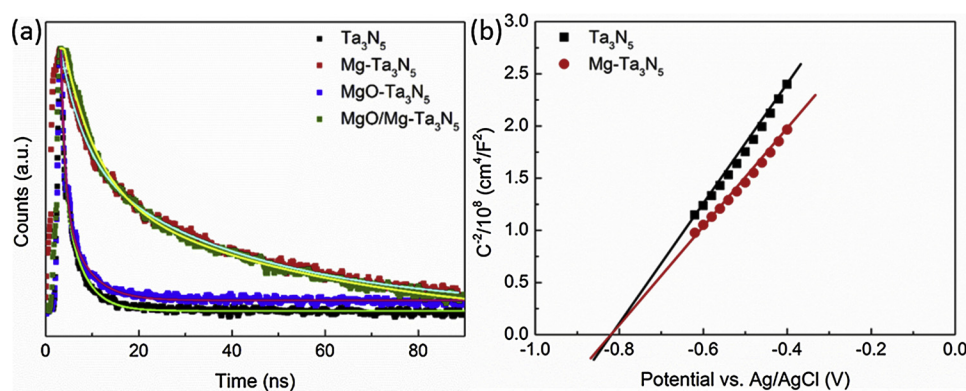


Fig. 4. (a) Time-resolved fluorescence decay spectra of samples Ta₃N₅, Mg-Ta₃N₅, MgO-Ta₃N₅ and MgO/Mg-Ta₃N₅. (b) Mott-Schottky plot of Ta₃N₅ and Mg-Ta₃N₅ in dark with 1 M NaOH aqueous solution as electrolyte.

around 2.63 nm, 2.04 nm and 1.33 nm respectively (Fig. S12 ESI[†]). The particle size of Pt on Ta₃N₅ hollow spheres was smaller than that of the bulk counterpart, which could be attributed to the higher surface area of hollow spheres. After covering a thin layer of MgO on the surface, the particle size of Pt further decreased to 1.33 nm, demonstrating the improved interfacial charge transfer [23,37]. The small particle size of Pt suggests a high ratio of Pt atoms exposed on the surface, which not only enhances the utilization of Pt cocatalyst but also promotes the catalytic reactions.

To evaluate the effect of reduced charge recombination on photocatalytic activity of Ta₃N₅ photocatalysts, photocatalytic H₂ evolution reaction were carried out for all samples (Fig. 5a). The generation of H₂ was detected for all samples from an aqueous solution containing methanol (10 vol%) as electron donor under irradiation of simulated sunlight. Compared with bulk Ta₃N₅, all the samples show improved H₂ evolution rates. Due to efficient suppression of bulk recombination, Mg-Ta₃N₅ hollow spheres exhibit a H₂ evolution rate of 11 μmol h⁻¹ while the value for bulk Ta₃N₅ is only 1.54 μmol h⁻¹. When further reducing the interfacial recombination with the MgO nano-layer, the H₂ evolution rate of MgO/Mg-Ta₃N₅ reaches to 29.4 μmol h⁻¹. Encouragingly, the final product Pt/CoO_x/MgO/Mg-Ta₃N₅ photocatalyst stands out, exhibiting the best performance for H₂ evolution, reaching 56.3 μmol h⁻¹. Remarkably, this H₂ production rate is ca. 13 times higher than that of the reference Pt/Ta₃N₅ hollow spheres, which is attributed to the synergistic suppression of charge recombination in bulk, interface and on surface of Ta₃N₅. Furthermore, there is no obvious decrease of photocatalytic H₂ evolution activity under 5 h illumination, indicating the excellent stability of Pt/CoO_x/MgO/Mg-Ta₃N₅ photocatalyst (Fig. S13, ESI[†]). The effect of each strategy on the H₂ evolution activity for Pt/CoO_x/MgO/Mg-Ta₃N₅ photocatalyst is summarized in Fig. 5b. Compared with its bulk counterpart, the increased ratio of H₂

generation rate for Mg dopants and hollow structure, MgO nano-layer, and dual co-catalysts are 7.6, 17.3 and 10.1, respectively. The MgO nano-layer is the most effective strategy, nearly as six times as that of hollow structure, due to efficient charge transfer between co-catalysts and Ta₃N₅ and passivation of surface defects. Such a result indicates that interface charge recombination plays a crucial role in influencing the photocatalytic performance, possibly owing to high specific surface area of Ta₃N₅ hollow spheres. In addition, the dual-cocatalyst strategy ranks second for the contribution to H₂ production performance, demonstrating the important role of surface charge separation in the whole photocatalytic process. Noticeably, through the combination of hollow structure, Mg doping, MgO surface modification and dual-cocatalyst strategies, the H₂ evolution rate is remarkably improved compared with that modified by a single strategy. This demonstrates that a combined strategy in suppressing the charge recombination in bulk, interface and on surface is an effective approach to enhance the photocatalytic efficiency of Ta₃N₅ photocatalyst. However, the apparent quantum efficiency (AQE) of this photocatalyst under 400 nm is still moderate (0.31%), possibly due to the low visible-light conversion efficiency of Ta₃N₅ photocatalyst. Therefore, more effort will be made to enhance the utilization efficiency of visible light in the future work.

4. Conclusion

To sum up, the combination of multiple strategies to design new Ta₃N₅ photocatalyst for efficient solar H₂ generation has been demonstrated. Hollow structure, Mg²⁺ doping, Pt/CoO_x cocatalysts for redox reactions and MgO interfacial coating cooperate to reduce the bulk, surface and interface recombination problems in Ta₃N₅ photocatalyst simultaneously. Due to the effective suppression of photo-generated charge recombination, this Pt/CoO_x/MgO/Mg-Ta₃N₅ photocatalyst

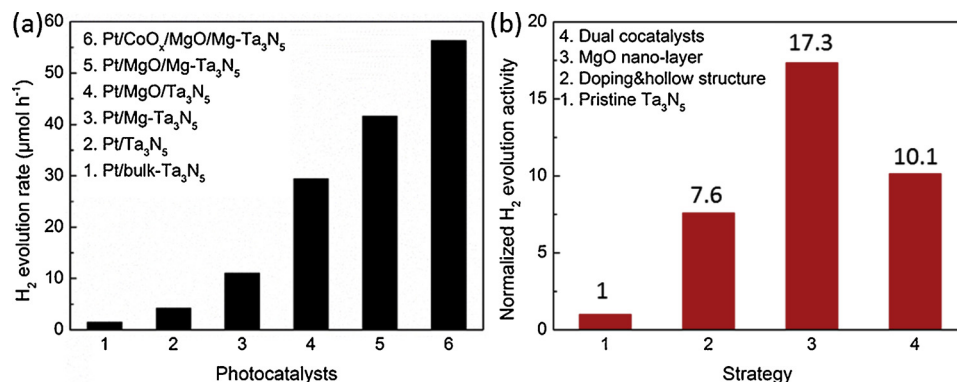


Fig. 5. (a) H₂ evolution rate of samples Pt/Ta₃N₅, Pt/Mg-Ta₃N₅, Pt/MgO-Ta₃N₅ and Pt/CoO_x/MgO/Mg-Ta₃N₅. (b) Summary of the contribution of each strategy to the H₂ evolution performance for Pt/CoO_x/MgO/Mg-Ta₃N₅ photocatalyst under simulated sunlight.

exhibits drastically improved photocatalytic H_2 evolution of $56.3 \mu\text{mol h}^{-1}$ under simulated sunlight, which apparently higher than that of $\text{Pt/Ta}_3\text{N}_5$ hollow spheres. Detailed characterization also revealed the contribution of each individual towards photocatalytic performance in this deliberately designed photocatalysts, which could be important to better understand the structure-property relation in the complex photocatalysis process. The synergistic approach can be generally applied to optimize the performance of other photocatalysts. It is believed that this work would shed light on the design and development of highly efficient photocatalysts for solar energy conversion.

Acknowledgments

The authors would like to acknowledge the financial support from Australian Research Council through its DP and FF programs. This work was performed in part at the Queensland node of the Australian National Fabrication Facility. M. Xiao acknowledges the support from the Australian Government Research Training Program Scholarship.

Appendix A. Supplementary data

Supplementary material related to this article can be found, in the online version, at doi:<https://doi.org/10.1016/j.apcatb.2019.01.053>.

References

- [1] Y. Tachibana, L. Vayssieres, J.R. Durrant, *Nat. Photonics* 6 (2012) 511.
- [2] A. Fujishima, K. Honda, *Nature* 238 (1972) 37.
- [3] N.S. Lewis, *Science* 315 (2007) 798–801.
- [4] L. Hammarström, S. Hammes-Schiffer, *Acc. Chem. Res.* 42 (2009) 1859–1860.
- [5] H. Go, I. Akio, T. Tsuyoshi, K.J. N, H. Michikazu, D. Kazunari, *Chem. Lett.* 31 (2002) 736–737.
- [6] P. Zhang, J. Zhang, J. Gong, *Chem. Soc. Rev.* 43 (2014) 4395–4422.
- [7] M. Xiao, S. Wang, S. Thaweesak, B. Luo, L. Wang, *Engineering* 3 (2017) 365–378.
- [8] W.-J. Chun, A. Ishikawa, H. Fujisawa, T. Takata, J.N. Kondo, M. Hara, M. Kawai, Y. Matsumoto, K. Domen, *J. Phys. Chem. B* 107 (2003) 1798–1803.
- [9] J. Li, N. Wu, *Catal. Sci. Technol.* 5 (2015) 1360–1384.
- [10] Y. He, James E. Thorne, Cheng H. Wu, P. Ma, C. Du, Q. Dong, J. Guo, D. Wang, *Chem* 1 (2016) 640–655.
- [11] A. Ziani, E. Nurlaela, D.S. Dhawale, D.A. Silva, E. Alarousu, O.F. Mohammed, K. Takanabe, *Phys. Chem. Chem. Phys.* 17 (2015) 2670–2677.
- [12] D. Wang, T. Hisatomi, T. Takata, C. Pan, M. Katayama, J. Kubota, K. Domen, *Angew. Chem. Int. Ed.* 52 (2013) 11252–11256.
- [13] J. Wang, A. Ma, Z. Li, J. Jiang, J. Feng, Z. Zou, *Phys. Chem. Chem. Phys.* 17 (2015) 8166–8171.
- [14] J. Xiong, C. Han, Z. Li, S. Dou, *Sci. Bull.* 60 (2015) 2083–2090.
- [15] G. Liu, L. Wang, H.G. Yang, H.-M. Cheng, G.Q. Lu, *J. Mater. Chem.* 20 (2010) 831–843.
- [16] M. Xiao, B. Luo, M. Lyu, S. Wang, L. Wang, *Adv. Energy Mater.* 8 (2018) 1701605-n/a.
- [17] K. Kishida, T. Watanabe, *J. Ceram. Soc. Jpn.* 122 (2014) 156–160.
- [18] Y. Kado, C.-Y. Lee, K. Lee, J. Muller, M. Moll, E. Spiecker, P. Schmuki, *Chem. Commun.* 48 (2012) 8685–8687.
- [19] R. Gao, S. Zhou, M. Chen, L. Wu, *J. Mater. Chem.* 21 (2011) 17087–17090.
- [20] Y. Li, T. Takata, D. Cha, K. Takanabe, T. Minegishi, J. Kubota, K. Domen, *Adv. Mater.* 25 (2013) 125–131.
- [21] S. Grigorescu, B. Bärhausen, L. Wang, A. Mazare, J.E. Yoo, R. Hahn, P. Schmuki, *Electrochem. Commun.* 51 (2015) 85–88.
- [22] J. Seo, T. Takata, M. Nakabayashi, T. Hisatomi, N. Shibata, T. Minegishi, K. Domen, *J. Am. Chem. Soc.* 137 (2015) 12780–12783.
- [23] S. Chen, Y. Qi, Q. Ding, Z. Li, J. Cui, F. Zhang, C. Li, *J. Catal.* 339 (2016) 77–83.
- [24] S. Chen, S. Shen, G. Liu, Y. Qi, F. Zhang, C. Li, *Angew. Chem. Int. Ed.* 54 (2015) 3047–3051.
- [25] J. Sun, J. Zhang, M. Zhang, M. Antonietti, X. Fu, X. Wang, *Nat. Commun.* 3 (2012) 1139.
- [26] X. Sun, Y. Li, *Angew. Chem. Int. Ed.* 43 (2004) 3827–3831.
- [27] Y. Li, F. Li, X. Li, H. Song, Z. Lou, Z. Ye, L. Zhu, *Nano Energy* 19 (2016) 437–445.
- [28] Y. Li, X. Cheng, X. Ruan, H. Song, Z. Lou, Z. Ye, L. Zhu, *Nano Energy* 12 (2015) 775–784.
- [29] S. Hwang, M.C. Lee, W. Choi, *Appl. Catal. B-Environ.* 46 (2003) 49–63.
- [30] L. Pei, Z. Xu, Z. Shi, H. Zhu, S. Yan, Z. Zou, *J. Mater. Chem. A* 5 (2017) 20439–20447.
- [31] Z. Wang, Y. Qi, C. Ding, D. Fan, G. Liu, Y. Zhao, C. Li, *Chem. Sci.* 7 (2016) 4391–4399.
- [32] M. Xiao, B. Luo, S. Wang, L. Wang, *J. Energy Chem.* 27 (2018) 1111–1123.
- [33] E. Nurlaela, M. Harb, S. del Gobbo, M. Vashishta, K. Takanabe, *J. Solid State Chem.* 229 (2015) 219–227.
- [34] X. Lai, J.E. Halpert, D. Wang, *Energy Environ. Sci.* 5 (2012) 5604–5618.
- [35] M. Xiao, Z. Wang, M. Lyu, B. Luo, S. Wang, G. Liu, H.-M. Cheng, L. Wang, *Adv. Mater.* 0 (2018) 1801369.
- [36] Y. Xie, Y. Wang, Z. Chen, X. Xu, *ChemSusChem* 9 (2016) 1403–1412.
- [37] Y. Kang, Y. Yang, L.-C. Yin, X. Kang, L. Wang, G. Liu, H.-M. Cheng, *Adv. Mater.* 28 (2016) 6471–6477.